

Effects of single synthetic jet on turbulent boundary layer

Jin-Hao Zhang(张津浩)1, Biao-Hui Li(李彪辉)1, Yu-Fei Wang(王宇飞)1, and Nan Jiang(姜楠)1,2,†
Citation: Chin. Phys. B, 2022, 31 (7): 074702 DOI: 10.1088/1674-1056/ /ac4bd0
Journal homepage: http://cpb.iphy.ac.cn; http://iopscience.iop.org/cpb

What follows is a list of articles you may be interested in

Experimental investigation on drag reduction in a turbulent boundary layer with a submerged synthetic jet

Biao-Hui Li(李彪辉), Kang-Jun Wang(王康俊), Yu-Fei Wang(王宇飞), and Nan Jiang(姜楠)
Chin. Phys. B, 2022, 31 (**2**): 024702. DOI: 10.1088/1674-1056/ac0da6

Influence of uniform momentum zones on frictional drag within the turbulent boundary layer

Kangjun Wang(王康俊) and Nan Jiang(姜楠)
Chin. Phys. B, 2021, 30 (**3**): 034703. DOI: 10.1088/1674-1056/abc7a6

Effect of high-or low-speed fluctuations on the small-scale bursting events in an active control experiment

Xiao-Tong Cui(崔晓通), Nan Jiang(姜楠), and Zhan-Qi Tang(唐湛棋)
Chin. Phys. B, 2021, 30 (**1**): 014702. DOI: 10.1088/1674-1056/abc7a9

Coherent structures over riblets in turbulent boundary layer studied by combining time-resolved particle image velocimetry (TRPIV), proper orthogonal decomposition (POD), and finite-time Lyapunov exponent (FTLE)

Shan Li(李山), Nan Jiang(姜楠), Shaoqiong Yang(杨绍琼), Yongxiang Huang(黄永祥), Yanhua Wu(吴彦华)
Chin. Phys. B, 2018, 27 (**10**): 104701. DOI: 10.1088/1674-1056/27/10/104701

Active control of wall-bounded turbulence for drag reduction with piezoelectric oscillators

Jian-Xia Bai(白建侠), Nan Jiang(姜楠), Xiao-Bo Zheng(郑小波), Zhan-Qi Tang(唐湛琪), Kang-Jun Wang(王康俊), Xiao-Tong Cui(崔晓通)
Chin. Phys. B, 2018, 27 (**7**): 074701. DOI: 10.1088/1674-1056/27/7/074701

Effects of single synthetic jet on turbulent boundary layer

Jin-Hao Zhang(张津浩)[1], Biao-Hui Li(李彪辉)[1], Yu-Fei Wang(王宇飞)[1], and Nan Jiang(姜楠)[1,2,†]

[1] *Department of Mechanics, School of Mechanical Engineering, Tianjin University, Tianjin* 300350, *China*
[2] *Key Laboratory of Modern Engineering Mechanics, Tianjin* 300350, *China*

(Received 9 December 2021; revised manuscript received 13 January 2022; accepted manuscript online 17 January 2022)

The turbulent boundary layer (TBL) is actively controlled by the synthetic jet generated from a circular hole. According to the datasets of velocity fields acquired by a time-resolved particle image velocimetry (TR-PIV) system, the average drag reduction rate of 6.2% in the downstream direction of the hole is obtained with control. The results of phase averaging show that the synthetic jet generates one vortex pair each period and the consequent vortex evolves into hairpin vortex in the environment with free-stream, while the reverse vortex decays rapidly. From the statistical average, it can be found that a low-speed streak is generated downstream. Induced by the two vortex legs, the fluid under them converges to the middle. The drag reduction effect produced by the synthetic jet is local, and it reaches a maximum value at $x^+ = 400$, where the drag reduction rate reaches about 12.2%. After the extraction of coherent structure from the spatial two-point correlation analysis, it can be seen that the synthetic jet suppresses the streamwise scale and wall–normal scale of the large scale coherent structure, and slightly weakens the spanwise motion to achieve the effect of drag reduction.

Keywords: turbulent boundary layer, synthetic jet, hairpin vortex, drag reduction

PACS: 47.85.lb, 47.85.ld, 47.27.nb, 47.27.De **DOI:** 10.1088/1674-1056/ac4bd0

1. Introduction

High efficiency and energy saving is one of the main goals of today's industrial development, and the flow resistance of fluid will cause great energy loss. The frictional resistance between the turbulent boundary layer and the wall is an important part of the flow resistance, so it is of great significance to reduce the friction drag by controlling the turbulence. The controlling methods can be divided into active control[1–5] and passive control[6–9] according to whether additional energy input is needed. Active control can actively adapt itself to changes in flow conditions through reasonable design to expand the applicable scope of drag reduction.

Park and Choi[10] investigated the effect of uniform blowing and suction from the slit on turbulent boundary layer (TBL) by direct numerical simulation (DNS) and found that the wall friction in the downstream direction of the slot decreases rapidly in the suction process while the opposite scenario occurs in the case of suction. The DNS results acquired by Kametani and Fukagata[11] show that the average influence of suction and blowing is drag reduction, and the blowing control effect is much stronger than the existing active control method. Keirsbulck *et al.*[12] found that blowing reduces the anisotropy of coherent structure in the near-wall region and the longitudinal integral length scale is inversely proportional to blowing velocity by using hot-wire velocimetry. Bai *et al.*[13] investigated that the drive wave generated by the piezoelectric ceramic actuator can produce a layer of highly structured streamwise vortex, which creates a barrier effect between the wall and the large-scale coherent structure to achieve the drag reduction effect.

Barton and Glezer[14] proposed that the synthetic jet is a planar turbulent jet formed by the interaction among a series of reversely rotating vortex pairs at the edge of the orifice plate through the periodic movement of the elastic diaphragm in a closed cavity. Park *et al.*[15] used PIV to study the effects of synthetic jets with different vibration frequencies and incident angles, and found that the drag reduction effect is not uniform under different circumstances. The results presented by Lasagna *et al.*[16] describe that the vortex structure generated by the synthetic method is intermittently distributed in the transient flow field and increases in percentage with frequency increasing, but not affected by the yaw angle. Berk *et al.*[17,18] found that the synthetic jet leads to local momentum loss in TBL, which is caused mainly by the vortex structure generated by the interaction between the synthetic jet and TBL. Iuso and Cicca[19] drew a conclusion that a large-scale longitudinal vortex structure with reverse rotation and periodic organization along the spanwise is generated by spanwise inclined circular synthetic jets. Chaudhry and Zhong[20] experimentally explored the flow characteristics of a single circular synthetic jet entering into laminar and turbulent boundary layers respectively, thus effectively studying the interaction between vortex and variable boundary layer.

According to the generating mechanism of hairpin vortex,[21] the research on artificial hairpin vortex has become popular. Now there are three artificial methods of producing hairpin vortices, *i.e.*, manufacturing a low-speed zone,[22] hemispherical induction,[23,24] and synthetic jets.[25]

†Corresponding author. E-mail: nanj@tju.edu.cn

© 2022 Chinese Physical Society and IOP Publishing Ltd

Previous studies have concluded that circular synthetic jet can produce drag reduction effect and periodically generate hairpin vortex structure. In this paper, the time-resolved particle image velocimetry (TR-PIV) system is utilized to implement the quantitative measurements of the flow field under the influence of the synthetic jet actuator (SJA), and the wall friction velocity is calculated by the single-pixel ensemble correlation[26,27] (SPEC). The velocity fields of streamwise-wall–normal plane and streamwise–spanwise plane are collected, and then the generation process of hairpin vortex and the drag reduction mechanism of synthetic jet in these two planes are studied. The rest of this paper is organized as follows. In Section 2, the experimental instruments and measurement methods are described. In Section 3, the generating process of hairpin vortex and the mechanism of drag reduction are investugated. Finally, some conclusions are drawn in Section 4 .

2. Experimental setup

The present experiments were carried out in the low-speed recirculating water channel facility at the Tianjin University. The channel was half-closed, creating a test section of 6.20 m×0.29 m×0.38 m (length×width×height as indicated in Fig. 1(a)). The bottom and the sidewalls of the test section was made of plexiglass to allow light access.

The researches were conducted in two parts, including the measurement of TBL on a classical plate and the measurement of that with SJA. In each part, the velocity field of the streamwise–wall–normal plane and the streamwise–spanwise plane were measured. As shown in Fig. 1, the side view and the top view of the two planes' shooting process are given respectively. In the experiment, the freestream turbulence intensity was less than 1.5% at a free-stream velocity $U_\infty = 0.255$ m/s, and the kinematic viscosity of water was $\upsilon = 9.6 \times 10^{-7}$ m^2/s. The turbulent boundary layers were developed on a smooth flat plate, and a 2-mm-diameter tripwire was fixed at 0.2 m in the downstream direction of the leading edge to stimulate into the full-developed TBL. The plate was 2.9-m long, 0.25-m wide, and 0.02-m thick, which had a 4:1 (long axis: short axis) elliptical leading edge. A circular hole with a diameter of 4 mm was made at the center line 2.45 m away from the leading edge. An actuator was mounted under a cavity at the bottom of the plate and generated the synthetic jet periodically through the hole after giving a sinusoidal signal with a fixed voltage and an excitation frequency (10 V and 26 Hz in the investigations, which was the working condition with the best drag reduction effect in order to study the drag reduction mechanism of synthetic jet). The size of the cavity and details of the actuator are shown in Fig. 1. In the present work, x, y, and z denote the streamwise direction, wall–normal direction, and spanwise direction, respectively; u, v, and w are defined as the instantaneous velocities in their respective directions; besides, the relevant fluctuation velocity components are given by u', v', and w'. The streamwise location and the spanwise location of the hole are defined as $x = 0$ and $z = 0$, and the upper surface of the plate in wall–normal direction is set to be $y = 0$.

The instantaneous velocity field was measure by the TR-PIV system. The flow was sprinkled by polyamide particles with a density of 1.03 g/mm^3 and an average diameter of 20 μm. A continuous laser sheet, with a thickness of 1 mm, was used to illuminate the test section.

When measuring the streamwise–wall–normal plane (x–y plane), the laser illuminated the flow field vertically downwards and the laser plane through the hole was parallel to the direction of incoming flow. A Speed Sense 9072 12-bit charge-coupled device (CCD) camera #1 recorded the images from a direction perpendicular to the laser plane, which had a Nikon lens with a focal length of 60 mm. The camera's resolution was set to be 1280 pixels×800 pixels and the particle image density was about 23 per 32 pixels×32 pixels. The field of view (FOV) was approximately 107 mm×67 mm in x direction and y direction and the left edge of FOV was 15-mm upstream of the orifice. In one set of data, a total of 41080 images were obtained with the sampling rate $f_s = 360$ Hz. Then these particle images were transformed into the corresponding velocity field by an iterative multi-grid cross-correlation algorithm. The adaptive correlation approach was used, with interrogation windows of 32 pixels×32 pixels and an overlap rate of 75%, resulting in a vector distance of 0.69 mm in the coordinate system. For camera #2 with a 200-mm Nikon lens, its resolution and sampling frequency were the same as those of camera #1. The size of its measurement area was about 26.06 mm×16.29 mm, and the left edge of FOV was 15 mm in the downstream direction of the hole. The relevant spatial resolution was 0.0204 mm/pixel, which was adequate to record the flow in the viscous sublayer. The images captured by camera #2 were utilized to calculate the friction velocity by SPEC. Because of the very thin viscous sublayer, the areas that needed to be processed with SPEC was set to be 1280 pixels×80 pixels (26.06 mm×1.63 mm in the x direction and y direction).

When measuring the stream–spanwise plane (x–z plane), the laser surface was parallel to the plate on the side of the channel. The camera #1 captured the flow from above, and the other settings of it reminded unchanged. The FOV recorded was approximately 107 mm×67 mm in the x direction and the z direction, and its left edge was located 15-mm upstream of the orifice. The distance between the laser plane and the plate could be adjusted freely to acquire the velocity fields at two different heights (4.5 mm and 10.5 mm).

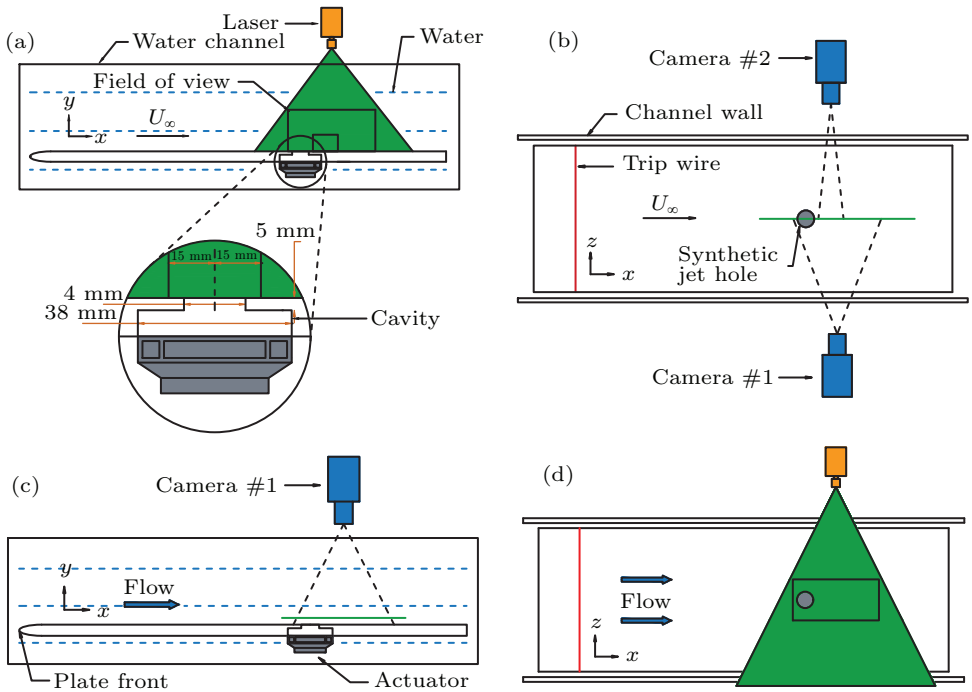


Fig. 1. Schematic diagram of experimental setup, showing [(a), (b)] streamwise–wall–normal plane, and [(c), (d)] stream–spanwise plane.

3. Results and discussion

3.1. Flow basic parameters

To describe the experimental conditions more clearly, the flow parameters of the boundary layer without control (00 V 00 Hz) under the condition of fully developed turbulent boundary layer state are listed in Table 1. The friction velocity $u_\tau = 11.21$ mm/s is fitted by the Spalding profile[28] which is in the following form:

$$y^+ = u^+ + \mathrm{e}^{-\kappa B}[\mathrm{e}^{\kappa u^+} - 1 - \kappa u^+ - (\kappa u^+)^2/2 - (\kappa u^+)^3/6], \quad (1)$$

with the log-law constants $\kappa = 0.41$ and $B = 5.2$; using the SPEC method and linear law fitting method, u_τ is obtained to be 11.22 mm/s. The goodness of fit acquired by these two measurements is greater than 0.9996 and the results are basically consistent. Then, $u_\tau = 11.21$ mm/s is defined as the standard value to be utilized later. Figures 2(a) and 2(b) show the profiles of mean streamwise velocity and the intensity of turbulence in x–y plane, respectively. For comparison, the DNS data of the zero-pressure gradient TBL obtained by Schlatter and Orlu[29] are put in these figures with similar values of Re_τ. Obviously, the two sets of data are basically the same, which indicates that a fully developed TBL has been obtained. In the diagram, both velocity and length are dimensionless by inner-scale units, which are $u^+ = u/u_\tau$ and $y^+ = yu_\tau/\upsilon$.

The thickness δ of boundary layer is based on a height of $0.99U_\infty$. The skin friction stress is calculated from

$$\tau_\mathrm{w} = \rho u_\tau^2, \quad (2)$$

where the density ρ of water is 998 kg/m^3. The corresponding skin friction coefficient is described by the following formula:

$$C_\mathrm{f} = 2\tau_\mathrm{w}/\rho U_\infty^2 = 2u_\tau^2/U_\infty^2. \quad (3)$$

Then, the drag reduction rate can be defined as

$$DR = (1 - C_\mathrm{f1}/C_\mathrm{f0}) \times 100\%, \quad (4)$$

where C_f0 represents the frictional factor without control, and C_f1 denotes that after control, the computing method of Re_τ is obtained according to

$$Re_\tau = u_\tau \delta/\upsilon. \quad (5)$$

Table 1. Flow parameters of boundary layer.

Variable	Parameter	Simulation value
u_∞	free-stream velocity	255 mm/s
u_τ	friction velocity	11.21 mm/s
τ_w	skin friction stress	0.1255 kg/(m·s^2)
C_f	skin friction coefficient	3.86×10^{-3}
δ	boundary layer thickness	46.0 mm
δ^*	displacement thickness	6.41 mm
δ_θ	momentum thickness	4.98 mm
H	shape factor	1.29
Re_τ	friction velocity Re number	537

According to the above, after using the synthetic jet control, the results are as follows: $u_\tau = 10.86$ mm/s calculated by the SPEC method, $\tau_\mathrm{w} = 0.1178$ kg/(m·s^2), $C_\mathrm{f1} = 3.63 \times 10^{-3}$, $DR = 6.2\%$. It can be found that under the influence of synthetic jet, the flow field shows the phenomenon of drag reduction of about 15 mm–41 mm in the downstream direction of the jet hole (x ranges from 15 mm to 41 mm).

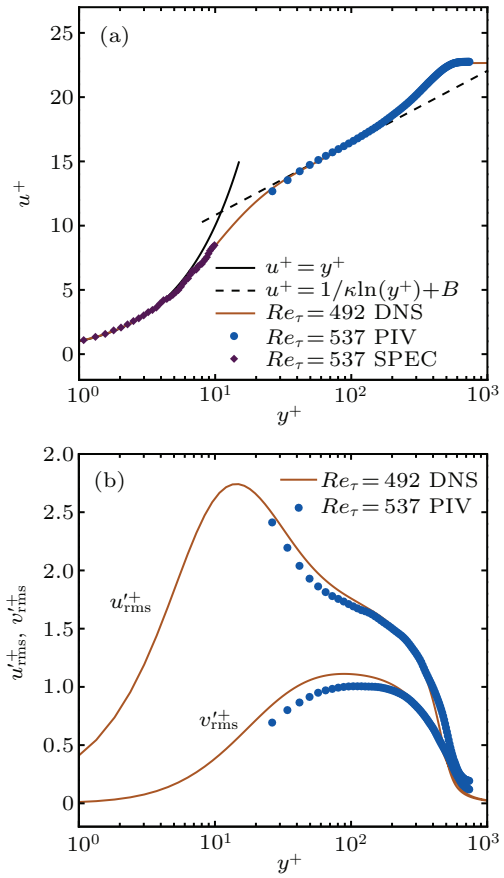


Fig. 2. Profiles of (a) mean streamwise velocity and (b) streamwise and wall–normal turbulent fluctuation intensity, with scatter points showing experimental data, and curves representing DNS results.

Figure 3 illustrates the viscous sublayer's mean streamwise velocity profiles normalized by the same inner-scale unit $u_\tau = 11.21$ mm/s. As can be seen from the figure, the viscous substrate is thickened after the synthetic jet control, which is the representative characteristic of drag reduction in TBL.

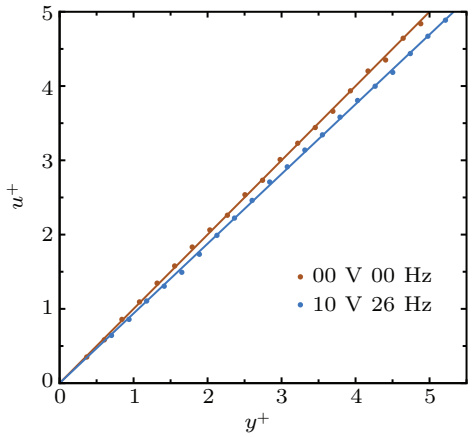


Fig. 3. Mean streamwise velocity profiles of viscous sublayers.

3.2. Phase average of flow field

The influence of the synthetic jet on the static flow field is presented in Fig. 4. The red dotted line shows where the value is zero. It can be found that the central region with positive wall–normal velocity and the two side regions with negative wall–normal velocity are generated by the jet flow. Obviously, the value and area of the former are larger than those of the latter. This is consistent with the conclusion obtained by Sane and Hirayama[30] that for the same mass flux, the average influence of blowing on the flow field is greater than that of suction. Strong shear can be seen from the dense contour lines between the middle and both sides, resulting in the generation of vortex structure.

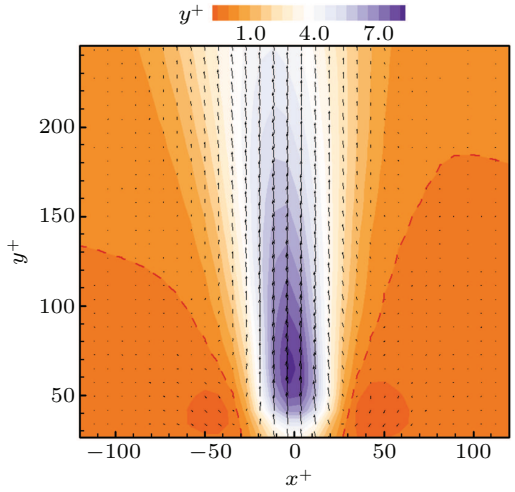


Fig. 4. Nephogram and vectors of time-averaged wall–normal velocity component in x–y plane without U_∞.

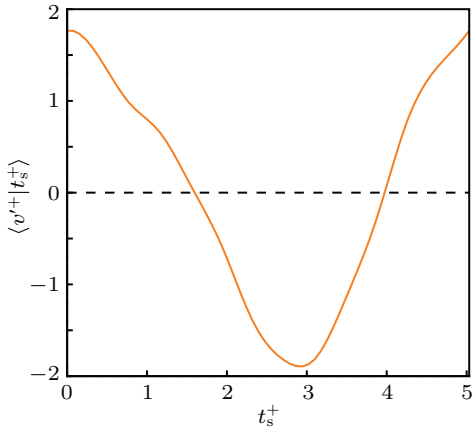


Fig. 5. Wall–normal fluctuation velocity curve of one period after phase averaging.

Periodic disturbance of the synthetic jet can produce periodic coherent structures of flow field which appear in the same place every cycle,[31] so they have a statistical distribution. In order to study the effect of the synthetic jet in one period, the phase averaging analysis of the flow field is carried out, which is obtained by averaging the superposition of velocity fields at the same phase time in different periods. Figure 5 shows the curve of wall–normal fluctuation velocity versus time of phase averaging at the location above the hole ($x^+ = 0$, $y^+ = 26$). The time of maximum wall–normal fluctuation velocity is set to be $t_s^+ = 0$, where t_s^+ is computed from

$$t_s^+ = t_s \rho u_\tau^2 / \delta_v, \tag{6}$$

here, t_s is the time in second during one period. It is observed that the full cycle time of the synthetic jet at a fixed frequency of 26 Hz is $t_s^+ \approx 5.032 = T$, and the absolute values of the maximum and minimum normal fluctuation velocities are almost equal.

Figure 6 illustrates the phase-averaged fluctuation velocity vector diagrams and the contours of vortex intensity Λ_{ci} in streamwise–wall–normal plane without U_∞, where the values of time t_s^+ are 0, $T/6$, $2T/6$, $3T/6$, $4T/6$, $5T/6$ respectively. The solid red line indicates that Λ_{ci} is 5. The expression of Λ_{ci} is given by

$$\Lambda_{ci} = \lambda_{ci}\,\mathrm{sign}\,(\omega) = \lambda_{ci}\,\omega/|\omega|, \tag{7}$$

where λ_{ci} is the imaginary part of the complex eigenvalue of velocity tensor, and ω denotes the vorticity perpendicular to the plane. We can see that under the influence of the synthetic jet, a complete spanwise vortex pair of reverse rotation will be generated near the hole every period. When t_s^+ is between 0 and about $2T/6$, the normal fluctuation velocity is positive, indicating blowing. As can be seen from the figure, the vortex pair spews out at a faster speed in this process, and the scope of vortex region becomes larger and larger. When t_s^+ changes from $2T/6$ to $4T/6$, the normal fluctuation velocity is negative, showing the phenomenon of suction. During this time, the height of the vortex pair basically does not change, which can be explained by the fact that the distance between the vortex pair and the hole is so far that the suction of the synthetic jet cannot pull it back. Furthermore, induced by this vortex pair, the flow field maintains the phenomenon that the normal velocity is high in the middle and low on both sides, thereby generating the next vortex pair in the next period.

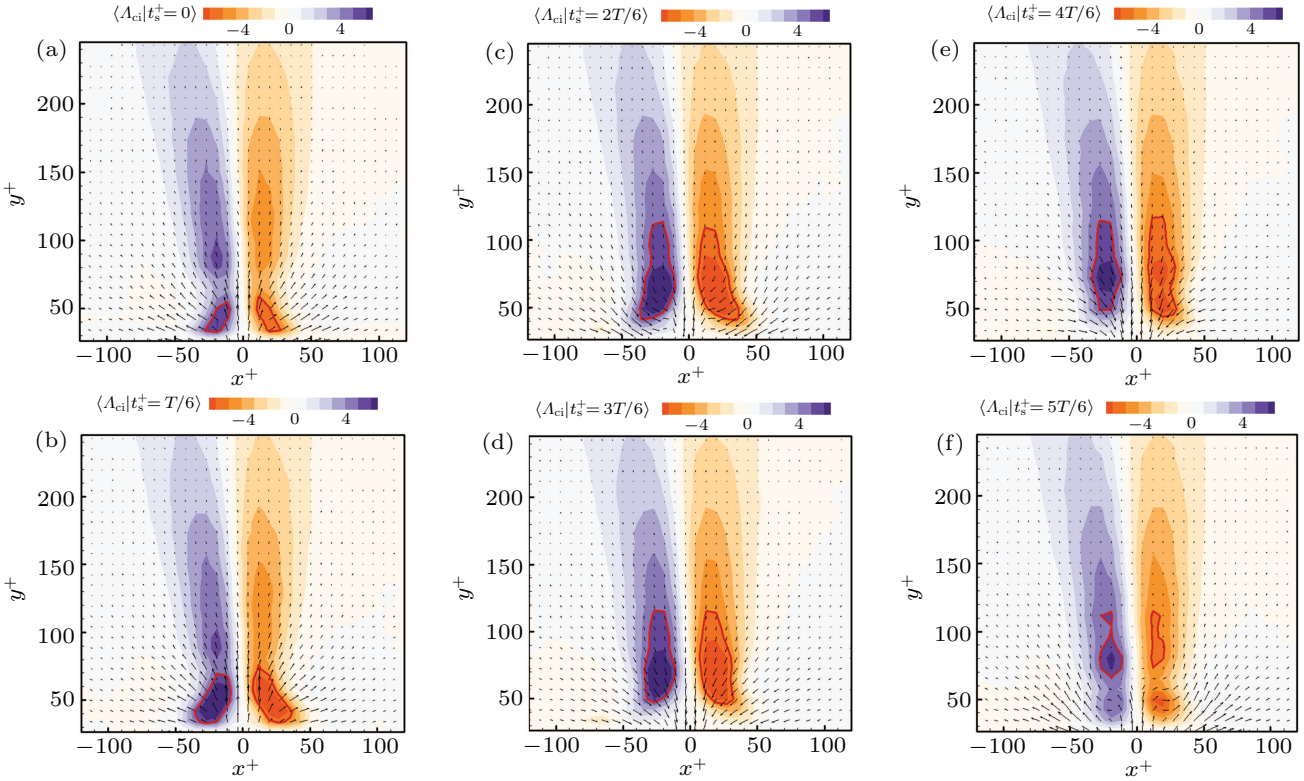


Fig. 6. Vectors of phase-averaged fluctuation velocity and the contours of vortex intensity at phase of (a) $t_s^+ = 0$, (b) $t_s^+ = T/6$, (c) $t_s^+ = 2T/6$, (d) $t_s^+ = 3T/6$, (e) $t_s^+ = 4T/6$, (f) $t_s^+ = 5T/6$ in x–y plane without U_∞.

In Fig. 7 the incoming flow velocity $U\infty$ is used on the basis of Fig. 6, and other conditions are the same as before. The solid red line shows the region where Λ_{ci} is 0. As can be found from these panels, there are almost no places where Λ_{ci} is negative. In other words, the reverse vortex generated upstream of the small hole decays so fast that it disappears from the FOV, while the consequent vortex in the downstream direction of the hole continues to evolve downstream under the action of free flow and its height gradually increases. The reason is that under the influence of U_∞, the shear strength of the TBL is enough to cancel the negative vorticity of the vortex pair and make it become a hairpin-like structure,[32] while the downstream side is subjected to a self-induced velocity, leading to its tilt in the direction of U_∞. After synthetic jet periodic disturbance, only three consecutive aligned forward vortices are observed in the figure due to the continuous attenuation of them in the process of development. Then a structure similar to hairpin vortex package is formed, where the forward vortex is the vortex head of hairpin vortex. The distance between each vortex depends on U_∞ and the frequency of the synthetic jet.[15]

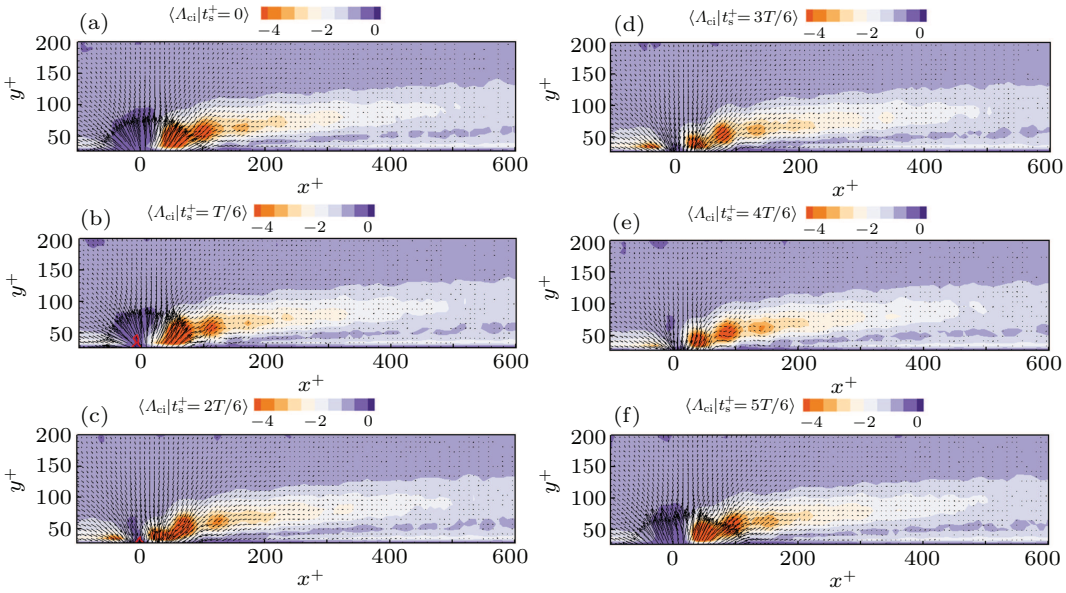


Fig. 7. Vectors of phase-averaged fluctuation velocity and contours of vortex intensity at phase of (a) $t_s^+ = 0$, (b) $t_s^+ = T/6$, (c) $t_s^+ = 2T/6$, (d) $t_s^+ = 3T/6$, (e) $t_s^+ = 4T/6$, and (f) $t_s^+ = 5T/6$ in x–y plane.

Figure 8 demonstrates the contours and vectors in streamwise–spanwise plane at $y^+ = 53$ corresponding to Fig. 7. It can be seen that in one period, a pair of counter-rotation normal vortices is created on either side of the hole, and it moves downstream at an almost constant rate. The reason is that the velocity generated by the synthetic jet is far less than U_∞, and the movement velocity of the vortex is mainly provided by U_∞. As shown in Figs. 8(b)–8(d), only two complete vortex pairs can be observed and they almost dissipate from the flow field at $x^+ \approx 150$. It is caused by the lifting action of the vortex structure which makes it gradually move away from the measuring plane. The distance between the two vortices in the vortex pair gradually increases in the process of downstream evolution. Combined with the phenomenon of the spanwise vortex, these are consistent with the evolution characteristics of the hairpin vortex, and the normal vortex pair is the two legs of the hairpin vortex.

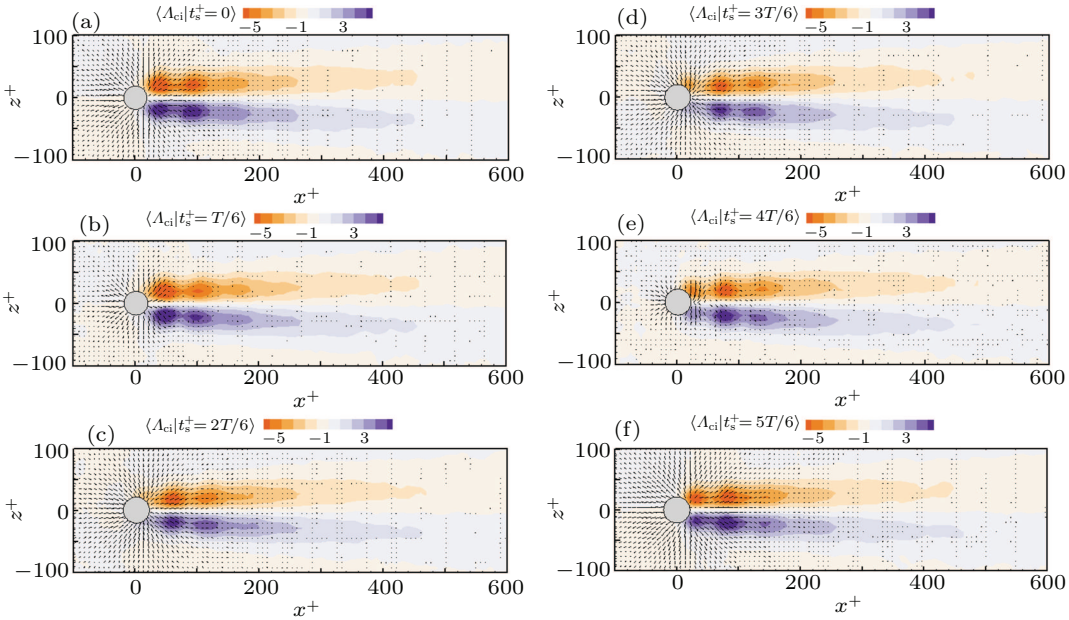


Fig. 8. Vectors of phase-averaged fluctuation velocity and contours of vortex intensity at phase of (a) $t_s^+ = 0$, (b) $t_s^+ = T/6$, (c) $t_s^+ = 2T/6$, (d) $t_s^+ = 3T/6$, (e) $t_s^+ = 4T/6$, (f) $t_s^+ = 5T/6$ in x–z plane at $y^+ = 53$.

3.3. Statistical average

After the control is applied to the flow field, the synthetic jet enters into the TBL along the wall–normal direction, and the ejected fluid has a low momentum in the streamwise direction. Therefore, after the drastic momentum exchange occurs, a large velocity deficit can be generated in the TBL.[33]

Figure 9 describes the time-averaged difference between control and non-control of streamwise velocity, and that of wall–normal velocity in streamwise–wall–normal plane. The zero isoline is marked by solid red line. According to Fig. 9(a), under the influence of the synthetic jet, most velocity deficit regions appear in the flow field with $y^+ < 150$, which are caused by the joint backward induction of the forward vortices. The velocity deficit reaches its maximum value at $x^+ \approx 85$, and then decreases continuously along the downstream direction. The contour line is similar to the ellipse inclined to the downstream direction. Observing the Fig. 9(b), there is a large normal velocity increment above the center of the orifice position. A big overlap between $\Delta v^+ > 0$ and $\Delta u^+ < 0$ occurs in the downstream direction of the outlet, which indicates that the synthetic jet makes the low-speed fluid at the bottom of the TBL manifest itself an upward movement trend, namely a large range of Q2 event. This is consistent with the phenomenon observed by Rathnasingham and Breuer.[34]

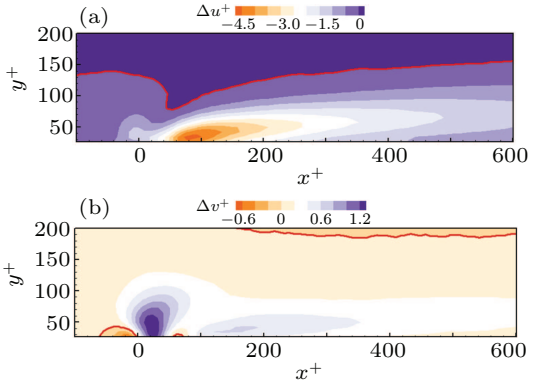


Fig. 9. Nephograms of (a) time-averaged difference between controlled and non-controlled streamwise velocity, and (b) time-averaged difference between controlled and non-controlled wall–normal velocity in x–y plane.

Figure 10 illustrates the time-averaged difference between control and non-control streamwise velocity, and the time-averaged difference between control and non-control spanwise velocity in streamwise–spanwise plane at $y^+ = 53$. The solid red line shows where $\Delta u^+ = 0$ and $\Delta w^+ = 0.2$ in Figs. 10(a) and 10(b) respectively. As can be found from Fig. 10(a), the streamwise velocity deficit area is symmetrically distributed along $z^+ = 0$. The velocity deficit reaches its maximum value at $x^+ \approx 85$ and gradually decreases downstream, which reflects that the synthetic jet generates a low-speed streak. The variation trend of zero isoline along x is almost consistent with the motion routes of the normal vortex pairs, which indicates that the low-speed streak is generated and developed under the induction of the vortex structure. As for Fig. 10(b), the ejection of the synthetic jet causes the outlet velocity to expand laterally. As the normal vortex pair gradually lifts away from the measurement plane, the graph manifests that under the induction of two hairpin vortex legs, the fluid below moves towards the middle.

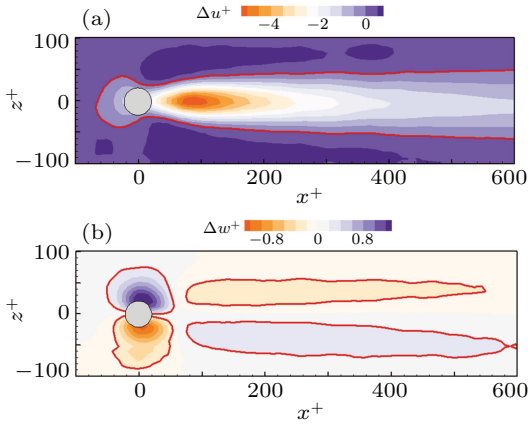


Fig. 10. Nephograms of (a) time-averaged difference between controlled and non-controlled streamwise velocity, and (b) time-averaged difference between controlled and non-controlled spanwise velocity in x–z plane at $y^+ = 53$.

3.4. Inspection of partial drag reduction

For studying the drag reduction strength of the synthetic jet at different streamwise positions, figure 11 depicts the variation of the ratio of wall friction coefficient C_{f1} with the control of the synthetic jet to coefficient C_{f0} without the control of the synthetic jet along the x direction. Because the selected streamwise distance is short, C_{f0} is regarded as a constant, which is 3.86×10^{-3} from the average value. Among them, the data used derive from the near-wall velocity field and are collected by camera #2, and the skin-friction drag coefficient is obtained by fitting with a linear law.

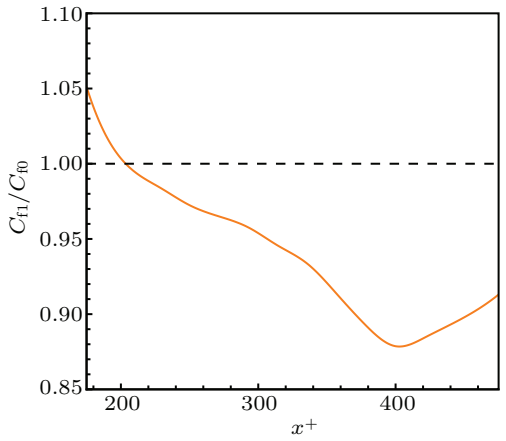


Fig. 11. Curve of skin-friction drag coefficient in x direction.

According to formula (4), when $C_{f1}/C_{f0} < 1$, the flow field is characterized by drag reduction, and the smaller the value, the better the drag reduction effect is. It can be seen from Fig. 11 that the wall friction resistance of the flow field increases with respect to no control scenario in the region where $x^+ < 200$ approximately, but the increment quickly dwindles to zero. At the downstream position, the synthetic jet begins to generate the drag reduction effect and reaches its maximum value at about $x^+ = 400$, where the drag reduction rate is about 12.2%.

In the further downstream direction, the effect gradually decreases as it keeps away from the synthetic jet control, which is similar to the result from Lu *et al.*[35] In total, the synthetic jet has a drag reduction effect on the local flow field and the effect is not uniform.

Figure 12 demonstrates the variation of the streamwise and normal fluctuation intensity in the x direction at $y^+ = 26$, where the subscripts 0, 1 represent non-control case and control case respectively. The results show that the rapid decrease of the fluctuation intensity at the position $x^+ < 200$ leads the skin-friction drag to drop sharply, and the reason for the large value is that the area is too close to the hole, which is more affected by disturbance. In the range of $x^+ > 200$, the synthetic jet restrains the streamwise fluctuation of the fluid so as to inhibit the streamwise momentum exchange and energy transport, and the inhibition effect reaches its maximum value at position $x^+ = 390$ which approximates to the extreme point of the drag coefficient. On the whole, the normal fluctuation intensity is always enhanced relative to no control case and gradually decreases until the value tends to 1 after leaving the disturbance range. The streamwise fluctuation intensity changes along the x direction in a similar way to the resistance coefficient, which indicates that one of the reasons for drag reduction is that the synthetic jet weakens the streamwise fluctuation intensity in the downstream direction of the orifice.

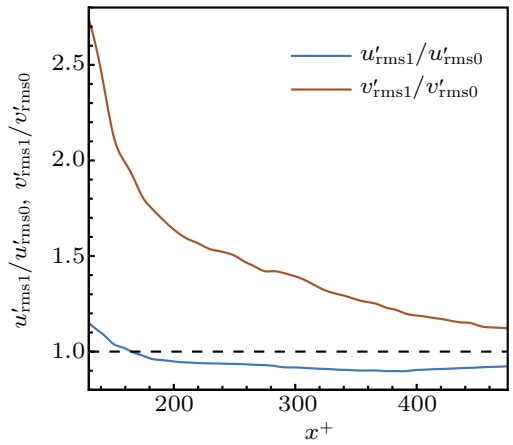


Fig. 12. Curves of turbulent fluctuation intensity in x direction at $y^+ = 26$.

3.5. Two-point correlation analysis

Coherent structure is the main mechanism for the maintenance, evolution and development of TBL, which plays an important role in transporting the turbulent energy and momentum. A large number of studies[36,37] on TBL show that there are coherent structures near the wall, such as streamwise vortices and hairpin vortices. They induce the surrounding fluid in the flow and form a high-speed or low-speed fluid region with a certain spatial scale correlation, which has a definite order in space. If the correlation or scale of the generated coherent region is weakened, the intensity and induction degree of the coherent structure are reduced, and then the resistance is reduced. In order to investigate the scale change of coherent structure after applying synthetic jet control, a spatial two-point correlation analysis[38,39] is carried out. In this part, two normal heights are selected, $y^+ = 53$ which is more affected by the synthetic jet and $y^+ = 123$ which is less affected by it.

The two-dimensional correlation function can obtain the scale information about the coherent motion in the plane and reveal the spatial morphology of the coherent structure in the boundary layer. The two-dimensional spatial correlation function of streamwise fluctuation velocity in streamwise–wall–normal plane used here is defined as

$$R_{u'u'}(\Delta x, y, y_{\mathrm{ref}}) = \frac{\overline{u(x, y_{\mathrm{ref}})\, u(x+\Delta x, y)}}{\sigma_{u'}(y_{\mathrm{ref}})\, \sigma_{u'}(y)}, \tag{8}$$

where y_{ref} is the normal position of the reference section, and $\sigma_{u'}$ is the root mean square value of streamwise fluctuation velocity u'. The above formula represents the correlation function between flow direction fluctuation velocity at each position in the flow field and that at the normal reference position.

Figure 13 describes a comparison between the two-dimensional correlated streamwise fluctuation velocities without and with the synthetic jet at position $x^+ = 430$, $y^+ = 53$, and $z^+ = 0$. The red dotted line represents the contour line $R_{u'u'} = 0.2$. The results show that there is large-scale coherent structure in the flow field, and the streamwise scale is larger than the normal and spanwise scale. Coherent structure has a certain angle with the direction of U_∞, which exhibits that the upstream of the structure is close to the wall and the downstream is far from the wall. The reason is that the coherent structure is constantly uplifted by the normal motion during the migration to the downstream direction, and the downstream development time is longer and in a higher height. In the streamwise–wall–normal plane, the dimensionless length and width of the contour lines marked are about 780 and 230 without control, and 510 and 140 with control. It is observed that the streamwise and normal scale of the coherent structure are more inhibited by the synthetic jet. In streamwise–spanwise plane, the change of the spanwise scale is not obvious.

Figure 14 demonstrates the two-point correlation results at position $x^+ = 430$, $y^+ = 123$, and $z^+ = 0$ corresponding to Fig. 11. Under the influence of the synthetic jet, the two scales change from 880, 320 to 680, 235 approximately, but the inhibition extent is less than the previous one. There is also no obvious change on a spanwise scale. This indicates that as the normal height is gradually away from the control of the synthetic jet, the inhibition on the streamwise and normal scale of the coherent structure will be weakened.

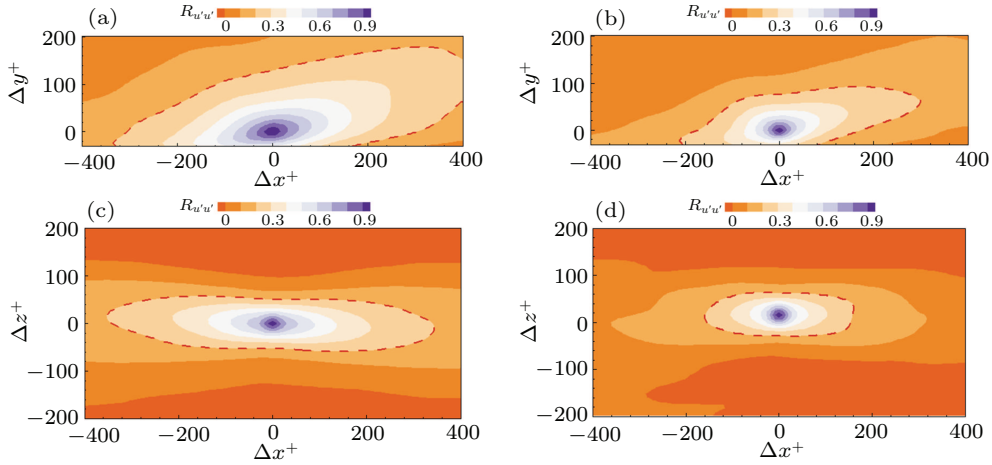


Fig. 13. Nephograms of spatial two-point correlation of the streamwise fluctuation velocity with (a) non-control and (b) control in x–y plane, and with (c) non-control and (d) control in x–z plane at position $x^+ = 430$, $y^+ = 53$, and $z^+ = 0$.

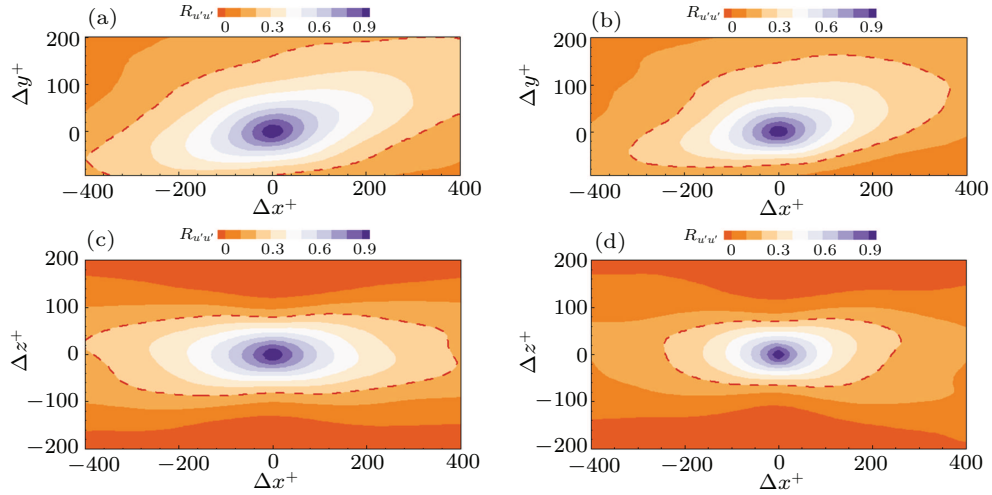


Fig. 14. Nephograms of spatial two-point correlation of streamwise fluctuation velocity with (a) non-control and (b) control in x–y plane, and with (c) non-control and (d) control in x–z plane at position $x^+ = 430$, $y^+ = 123$, and $z^+ = 0$.

Figure 15 shows the curves of the correlation coefficient versus spanwise position along the line $\Delta x^+ = 0$, clearly showing the changes of the spanwise scale. The results describe that the scale is suppressed on both sides, and a little more at the top.

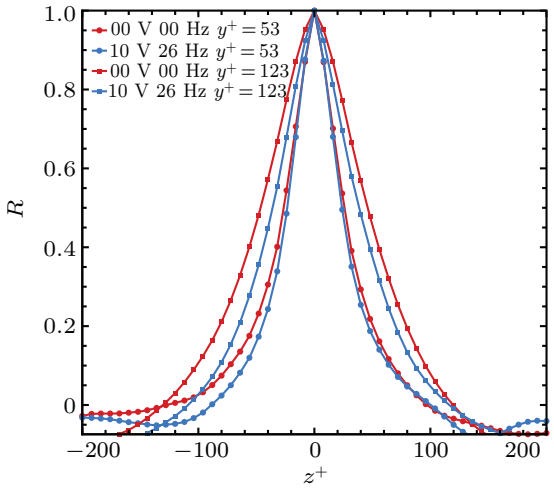


Fig. 15. Curves of correlation coefficient distribution in spanwise direction.

In general, the synthetic jet inhibits not only the downstream migration of coherent structures, but also their normal uplift and slightly weakens their spanwise motion, thus achieving the effect of drag reduction.

4. Conclusions

A 2D TR-PIV is utilized to collect the velocity field of the TBL in x–y plane and x–z plane. The friction velocity is calculated by the SPEC algorithm, and the average drag reduction rate is about 6.2%, when x^+ changes from 175 to 475 downstream of the jet opening. The time-averaged normal velocity generated by the synthetic jet in a stationary fluid is positive in the middle and negative on both sides, and there are strong shear forces at the junction.

The phase average analysis of synthetic jet with and without incoming flow are carried out. The results show that the period of the synthetic jet at the input frequency of 26 Hz is $t_s^+ \approx 5.032$, and a pair of spanwise vortices with opposite rotation directions is generated every period. In addition, the synthetic jet cannot suck back the vortex pairs that have been

blown out in the suction stage. Through the influence of u_∞, the reverse vortex upstream of the hole decays quickly, while the downstream consequent vortex continues to develop downstream into a structure similar to the hairpin vortex. In the process of its further development downstream, the vortex head rises continuously and the two vortex legs move to both sides. Under the continuous action of synthetic jet, the hairpin vortex packet structure composed of three hairpin vortices can be observed.

By subtracting the velocity field after time-averaging with control from that without control, it can be seen that the synthetic jet produces a large area of Q2 event and a low-speed streak downstream of the hole. Induced by two hairpin vortex legs, the fluid below them converges to the middle.

Under the influence of the synthetic jet, the flow field generates local drag reduction effect. Under this experimental condition, the effect reaches its maximum value at $x^+ = 400$, when the drag reduction rate reaches about 12.2%. The inhibition of the streamwise fluctuation intensity by the synthetic jet is also a reason for drag reduction.

The spatial two-point correlation analysis is used for the regions with two heights. The results illustrate that the synthetic jet can significantly inhibit the streamwise scale and normal scale of the large-scale coherent structure, and slightly weaken its spanwise motion. When the normal height is gradually away from the influence of the synthetic jet, the inhibition effect on the former is obviously weakened, while that on the latter is slightly enhanced. Finally, under the action of the synthetic jet, the drag reduction effect of flow field is obtained.

Acknowledgements

Project supported by the National Natural Science Foundation of China (Grant Nos. 11732010, 11972251, 11872272, 11902218, and 12172242) and the National Key Research and Development Program of the Ministry of Science and Technology, China (Grant No. 2018YFC0705300).

References

[1] Deng B Q and Xu C X 2012 *J. Fluids Mech.* **710** 234
[2] Jacobson S A and Reynolds W C 1998 *J. Fluids Mech.* **360** 179
[3] Kim J 2003 *J. Fluids Mech.* **15** 1093
[4] Jiang D W, Zhang H, Fan B C and Wang A H 2019 *Chin. Phys. B* **28** 054701
[5] Jiang D W, Zhang H, Fan B C, Zhao Z J, Gui M Y and Chen Z H 2019 *Ocean Eng.* **176** 74
[6] Min T, Yoo J Y, Choi H and Joseph D D 2003 *J. Fluids Mech.* **486** 213
[7] Min T and Kim J 2004 *Phys. Fluids* **16** L55
[8] Li S, Jiang N, Yang S Q, Huang Y X and Wu Y H 2018 *Chin. Phys. B* **27** 10
[9] Li L C, Liu B, Hao H L, Li L Y and Zeng Z X 2020 *Phys. Fluids* **32** 084103
[10] Park J and Choi H 1999 *Phys. Fluids* **11** 3095
[11] Kametani Y and Fukagata K 2011 *J. Fluids Mech.* **681** 154
[12] Keirsbulck L, Labraga L and Haddad M 2006 *Exp. Fluids* **40** 654
[13] Bai H L, Zhou Y, Zhang W G, Xu S J, Wang Y and Antonia R A 2014 *J. Fluids Mech.* **750** 316
[14] Smith B L and Glezer A 1998 *Phys. Fluids* **10** 2281
[15] Park Y S, Park S H and Sung H J 2003 *Exp. Fluids* **34** 697
[16] Lasagna D, Orazi M and Iuso G 2014 *Fluid Dyn. Res.* **46** 015501
[17] Berk T, Hutchins N, Marusic I and Ganapathisubramani B 2018 *J. Fluids Mech.* **856** 531
[18] Berk T, Gomit G and Ganapathisubramani B 2016 *J. Fluids Mech.* **804** 467
[19] Iuso G and Cicca G M 2007 *J. Turbul.* **8** 11
[20] Chaudhry I A and Zhong S 2014 *J. Vis.* **17** 101
[21] Kim H T, Kline S J and Reynolds W C 1971 *J. Fluids Mech.* **50** 133
[22] Acarlar M S and Smith C R 1987 *J. Fluids Mech.* **175** 43
[23] Acarlar M S and Smith C R 1987 *J. Fluids Mech.* **175** 1
[24] Tang Z Q and Jiang N 2012 *Sci. China-Phys. Mech.* **55** 118
[25] Suponitsky V, Cohen J and Bar-yoseph P Z 2005 *J. Fluids Mech.* **535** 65
[26] Westerweel J, Geelhoed P F and Lindken R 2004 *Exp. Fluids* **37** 375
[27] Shen J Q, Pan C and Wang J J 2014 *Sci. China-Phys. Mech.* **57** 1353
[28] Kendall A and Koochesfahani M 2008 *Exp. Fluids* **44** 773
[29] Schlatter P and Orlu R 2010 *J. Fluids Mech.* **659** 116
[30] Sano M and Hirayama N 1985 *Bull JSME* **28** 807
[31] Berk T and Ganapathisubramani B 2019 *J. Fluids Mech.* **870** 651
[32] Jabbal M and Zhong S 2008 *Int. J. Heat Fluid Flow* **29** 119
[33] Lardeau S and Leschziner M A 2011 *J. Fluids Mech.* **683** 172
[34] Rathnasingham R and Breuer K S 2003 *J. Fluids Mech.* **495** 209
[35] Lu L S, Li D, Gao Z H, Cao Z, Bai Y and Zheng J 2020 *Acta Mech. Sin.* **524** 57
[36] Head M R and Bandyopadhyay P 1981 *J. Fluids Mech.* **107** 297
[37] Robinson S K 1991 *J. Fluids Mech.* **23** 601
[38] Ganapathisubramani B, Hutchins N, Hambleton W T, Longmire E K and Marusic I 2005 *J. Fluids Mech.* **524** 57
[39] Volino R J, Schultz M P and Flack K A 2009 *J. Fluids Mech.* **635** 75